Engineered Science

RESEARCH PAPER

View Article Online

Zeolitic-imidazolate Framework (ZIF)@ZnCo-ZIF Core-shell Template-derived Co, N-doped Carbon Catalysts for Oxygen Reduction Reaction

Haiyan Yu, Liu Yang, Daojian Cheng* and Dapeng Cao *

Exposure of the active sites directly determines the catalytic activity of porous carbon electrocatalysts for oxygen reduction reaction (ORR). How to maximally expose these active sites in as-synthesized carbons is still a great challenge. Here we propose an efficient strategy to maximally expose the active sites of porous carbon catalysts, in which we use core-shell ZIF-8@ZnCo-ZIF (op-ZnCo-ZIF) as a precursor to synthesize Co, N-doped carbon catalysts (op-ZnCo-950) by pyrolysis. The low boiling metal Zn in the core-shell template can serve as the activation agent to yield the micropores and mesopores, and the cobalt in the shell is therefore dispersed well in the surface of as-synthesized carbons during the pyrolysis. As a result, the resultant op-ZnCo-950 exhibits a relatively high catalytic activity towards ORR with a half-wave potential of 0.846 V (*vs* RHE), and the higher methanol resistance and better stability than 20% Pt/C. This work provides an efficient core-shell template strategy for synthesis of carbon catalysts with highly exposed active sites for electrochemical applications including ORR, hydrogen evolution reaction and oxygen evolution reaction.

Keywords: Co, N-doped carbon electrocatalysts; Core-shell template; Oxygen reduction reaction; Zeolitic-imidazolate framework

Received 11th May 2018, Accepted 2nd June 2018

DOI: 10.30919/es8d729

1. Introduction

Fuel cells, as a highly efficient and environmentally friendly technology, can be considered as a promising solution of the severe energy shortage and environmental problems caused by traditional fossil fuels.[1–6] However, the extensive application of fuel cells is impeded by the sluggish cathodic oxygen reduction reaction (ORR) which is several orders slower than the anodic hydrogen oxidation reaction (HOR). Although Pt plays a state-of-the-art role in ORR,[7–10] it still hinders the large scale commercialization of fuel cells due to the scarcity, high price and negative properties (such as, low stability and low tolerance to methanol). Therefore, it is urgently required to develop highly efficient and cost-cheap non-noble metal catalysts for ORR. In recent decades, a lot of improvement has been made in the fields of non-precious ORR catalysts. In particular, Co- and Fe- involved catalysts show more fascinating potentialities than other transition metals like Zn, Ni, Mn and so on. Moreover, some Co- and Fe-based catalysts also showed comparable or even superior activities than commercial Pt/C in alkaline electrolyte.[11–25]

Metal-organic frameworks (MOFs), which contain well-distributed metal nodes and various links,[26,27] have structural diversity and good design ability, and were often chosen as ideal self-sacrificed precursors to prepare porous carbon materials through pyrolysis.[28,29] During the pyrolysis, metal nodes can be *in-situ* transformed into metal/metal oxide/metal carbide as active components, and organic ligands are changed into porous carbons as supporters inheriting the porosity. In this way, the electronical conductivity and stability can be ensured by the bonding between active sites and nanocarbons, rather than combining MOFs with a proper support by other methods.[30–32] Among the MOFs families, zeolitic imidazolate framework (ZIF) is the most shining series as precursors to prepare porous carbons,[33] due to the even distribution of metal and nitrogen-rich ligands.[13,14,29,34–45] In previous work, Zhang *et al.*[29] found that the low boiling point (907 °C) Zn atoms[40,46] can act as an activation agent to generate porous metal-free nitrogen-doped porous carbons. During the pyrolysis process, the reduction and evaporation of Zn species under high temperature can produce pores and increase the specific surface area (SSA). Nevertheless, metal-based catalysts usually exhibit better ORR performance than metal-free ones due to the formation of metal-N active sites and higher graphitic degree.[47] Accordingly, ZIFs containing Co and Fe metals have also been considered as templates to synthesize highly efficient non-precious metallic electrocatalysis,[12,39,41,48–50] where Co species in ZIF can generate Co-N_x moieties, Co nanoparticles (NPs) or CoO_x NPs beneficial for ORR.[32,37,43,46,51] However, a serious common problem is the aggregation of metallic species of the samples derived from Co- or Fe-ZIFs at high temperature, which would lead to low SSA.[37,38,52] Therefore, combining low boiling point metal Zn and high

Beijing Advanced Innovation Center for Soft Matter Science and Engineering, and State Key Lab of Organic-Inorganic Composites, Beijing University of Chemical Technology, Beijing 100029, People's Republic of China.
E-mail: chengdj@mail.buct.edu.cn, caodp@mail.buct.edu.cn

activity metal Co or Fe in a precursor is a good strategy to solve the problem. As a result, bimetal strategy[13,34,40,53] and core-shell structure[14,50,54] were proposed previously. For example, ZnCo-bimetal MOFs was used as a self-adjusted precursor to synthesize Co-N-C with little Co sinter.[13,55,56] And even single atom cobalt structure with precise N-coordination can be achieved as superior ORR catalysts.[40,57,58] Moreover, a core-shell structure containing ZnCo bimetal NPs was also used as an ideal precursor to synthesize an efficient electrocatalyst for both ORR and OER.[14,59] Generally, traditional ZIF core-shell structures were usually synthesized by epitaxial growth method which contains collection, clean, dry and dispersion of the core seed crystals before formation of core-shell materials,[60–62] which is a relatively complex method. Since ORR is an interfacial catalytic reaction, the accessibility of the active sites is significantly critical. The core-shell precursors can make the derived catalysts expose more active sites on the outer layer and therefore improve ORR performance. Thus, it is significant to use a facile method and special core-shell template to develop highly efficient ORR catalysts.

Here, we use a facile one-pot method to prepare a core-shell template with ZIF-8 as the core and bimetal ZnCo-ZIF as the shell (marked as op-ZnCo-ZIF), and then the op-ZnCo-ZIF is further adopted as a precursor to synthesize Co, N-doped porous carbons (marked as op-ZnCo-950), where the low boiling point metal Zn in the core and shell would be evaporated and acted as an activating agent to produce micropores and mesopores in the thermal treatment process, while the Co species in the shell would be retained in the surface of samples and maximally exposed as active sites. For comparison, we also use non-core-shell structure ZIF-67 as a precursor to synthesize ZIF-67-950 carbon sample in the same conditions. To highlight the importance of core-shell template, the intrinsic properties and ORR activities of the two samples of op-ZnCo-950 and ZIF-67-950 are investigated systematically. Finally, some conclusions are drawn, and some discussion is addressed.

2. Experimental section

The synthesis strategies of op-ZnCo-ZIF and op-ZnCo-950 were presented in Scheme 1, where the precursor of op-ZnCo-ZIF was synthesized by a facile one-pot method at room temperature. First, ZIF-8 was synthesized at room temperature by mixing $Zn(NO_3)_2$ and 2-methylimidazole (2-mIM) methanol solution and stirring for 2.5 h. Then, $Co(NO_3)_2{\cdot}6H_2O$ solution and additional 2-mIM solution were successively added into the previous milky solution containing ZIF-8 NPs, stirred for another 2.5 h. So, the residual Zn^{2+} ions, the newly added Co^{2+} ions and 2-mIM construct the shell of op-ZnCo-ZIF. Then, the violet op-ZnCo-ZIF sample can be obtained by filtering and washing by methanol for several times and dried in an oven of 60 °C for overnight. Finally, op-ZnCo-950 sample was obtained by the pyrolysis of op-ZnCo-ZIF under Ar flow at 950 °C for 2 hours. Obviously, the core of op-ZnCo-ZIF is ZIF-8 and its shell is bimetallic ZnCo-ZIF. In the op-ZnCo-ZIF, the special core ZIF-8 provides abundant Zn as an activating agent to produce micropores and mesopores at high temperature while the Co species in the shell would be retained in the surface of samples and maximally exposed as active sites. For comparison, a pure ZIF-67 was synthesized and then was carbonized to prepare ZIF-67-950 sample under Ar flow at 950 °C for 2 hours. Other detailed descriptions of preparation, characterization and electrochemical measurements were displayed in Supporting Information.

3. Results and discussion

The scanning electron microscope (SEM) image (Figure 1a) shows that op-ZnCo-ZIF is rhombic dodecahedral shape, and the diameter of the uniform particles is about 400-500 nm. The transmission electron microscope (TEM) image of op-ZnCo-ZIF in Figure 1b shows good correspondence with the SEM image. ZIF-8 and ZIF-67 have the same topology and structure parameters, which can be determined by single crystal X-ray diffraction (XRD) studies.[61,63] So it is easy for them to form bimetal structure or core-shell structure via epitaxial growth, and they will exhibit topological information identical to both ZIF-8 and ZIF-67 crystals. The well matching peaks of the wide-angle powder XRD (PXRD) graphs in Figure 1c suggested that op-ZnCo-ZIF definitely has the same topology with ZIF-8 and ZIF-67. Both elemental mapping and line scan (Figure 1d) show the complete distribution of Zn in the whole particle and the partial distribution of Co in the shell layer of the particle. Combining the results of PXRD and elemental mappings, we can infer that the

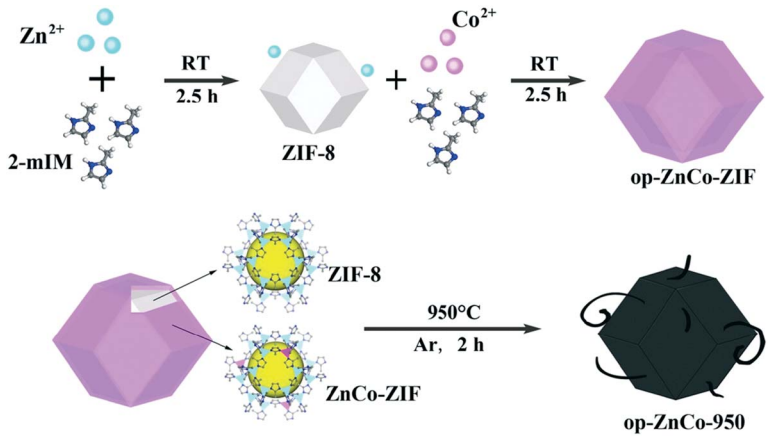

Scheme 1 Synthesis strategy of op-ZnCo-ZIF and op-ZnCo-950.

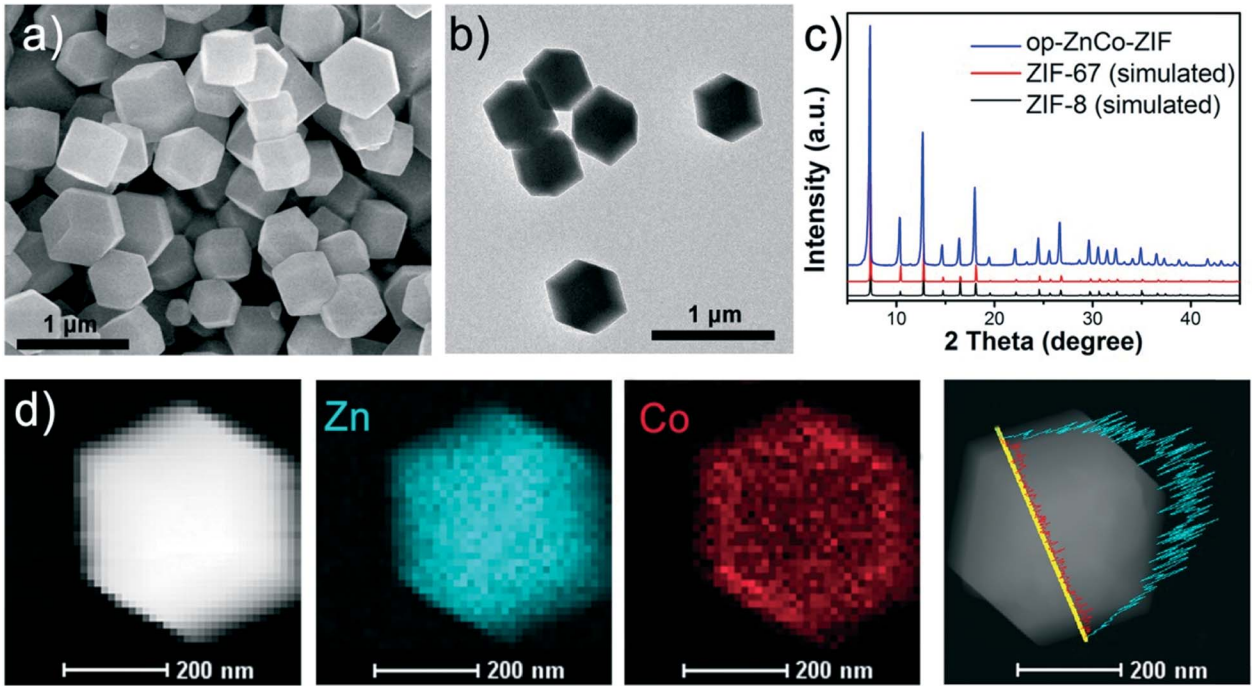

Fig. 1 (a) SEM and (b) TEM images of op-ZnCo-ZIF. (c) Wide-angle PXRD graphs of as-synthesized op-ZnCo-ZIF and simulated ZIF-67 and ZIF-8. (d) HAADF-STEM image, elemental mapping and line-scanning of the core-shell op-ZnCo-ZIF (blue: Zn, red: Co).

special structure of op-ZnCo-ZIF with ZIF-8 as the core and ZnCo-ZIF as the shell has been synthesized successfully by one-pot method.

The SEM image in Figure 2a reveals that the as-prepared op-ZnCo-950 basically remains the initial shape of op-ZnCo-ZIF. It can be seen from the HRTEM images of op-ZnCo-950 in Figure 2b and 2c that some carbon nanotubes (CNTs) were also formed. These CNTs were grown under the catalysis of Co NPs during the pyrolysis process.[60,64] Only a few small metal NPs can be seen in

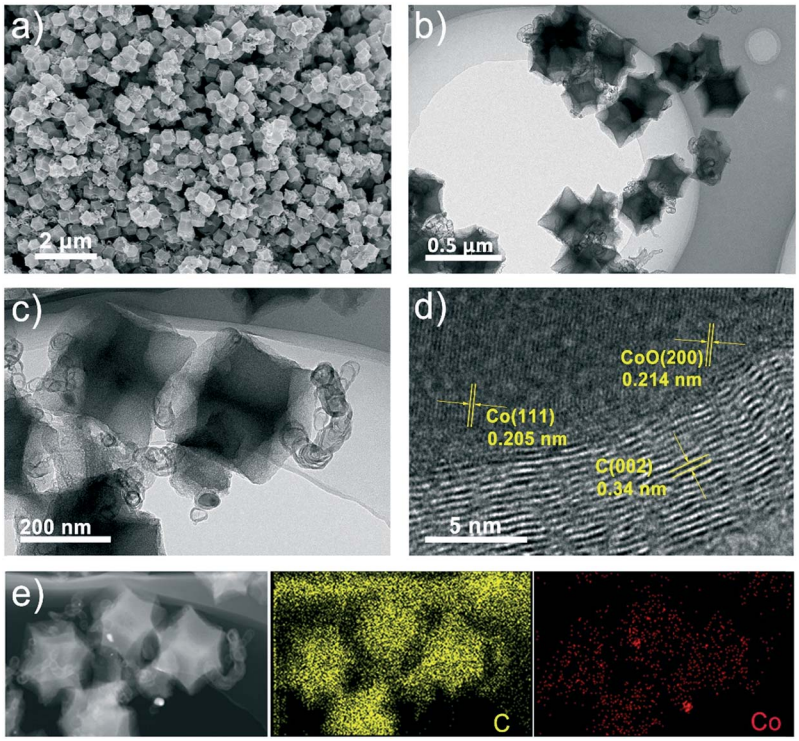

Fig. 2 (a) SEM and (b, c, d) HRTEM images and local magnification of op-ZnCo-950 at different scales. (e) HAADF-STEM image and elemental mapping of op-ZnCo-950 (yellow: C, red: Co).

Figure 2b, c, e. As shown in the high-magnification HRTEM image of the edge area of one metal NP (Figure 2d), the lattice fringes match with those of Co (111), CoO (200) and C (002), respectively. This reveals that the Co/CoO NPs are embedded in graphitic carbon layers. Moreover, the elemental mapping images of op-ZnCo-950 (Figure 2e) show uniform dispersion of cobalt and carbon as well, with only a few spots that show cobalt gathering. It suggests that cobalt was dispersed well, unlike the serious gathering status of ZIF-67-950 (Figure S1), which also confirms the advantages of core-shell template strategy.

To investigate the porosity of the samples, adsorption-desorption isotherms of N_2 at 77 K and pore size distribution (PSD) of op-ZnCo-950, op-ZnCo-ZIF, ZIF-67 and ZIF-67-950 are displayed in Figure 3a. We can see from the inset of Figure 3a that both op-ZnCo-ZIF and ZIF-67 have the higher N_2 adsorption amount than op-ZnCo-950 and ZIF-67-950. It can be found from Table S1 that after the thermal treatment, the BET SSA of ZIF-67-950 decreases sharply to 133.6 m^2 g^{-1} due to the shrink and collapse of ZIF-67 framework and aggregation of Co NPs, while op-ZnCo-950 still keeps a high BET SSA (1144 m^2 g^{-1}) and good hierarchical PSD with sufficient both micropores and mesopores, which are attributed to the special core-shell structure of op-ZnCo-ZIF, where the evaporation of metallic Zn is greatly beneficial for the formation of porous carbon materials. Zn species in the precursor not only enlarge the distance between two Co nodes in the shell to prevent Co aggregation, but also largely activate the whole carbon materials.

The PXRD graph of op-ZnCo-950 (Figure 3b) shows the two broad diffraction peaks at around 26° and 44°, which are assigned to the (002) and (101) diffractions of graphitic carbons. The diffraction peaks located at 44.2° and 51.5° are indexed to the (111) and (200) facets of Co crystal (PDF#15-0806). And the peaks at 36.5°, 42.4° and 61.5° are identical to the (111), (200) and (220) diffractions of CoO (PDF#43-1004), respectively. PXRD results are in accordance with the lattice fringes in Figure 2d.

The X-ray photoelectron spectroscopy (XPS) spectra of op-ZnCo-950 (Figure 3c) shows the N1s, C1s, O1s and Co2p peaks. The elemental content results of op-ZnCo-950 and ZIF-67-950 from XPS are summarized in Table S2. Op-ZnCo-950 presents a higher nitrogen

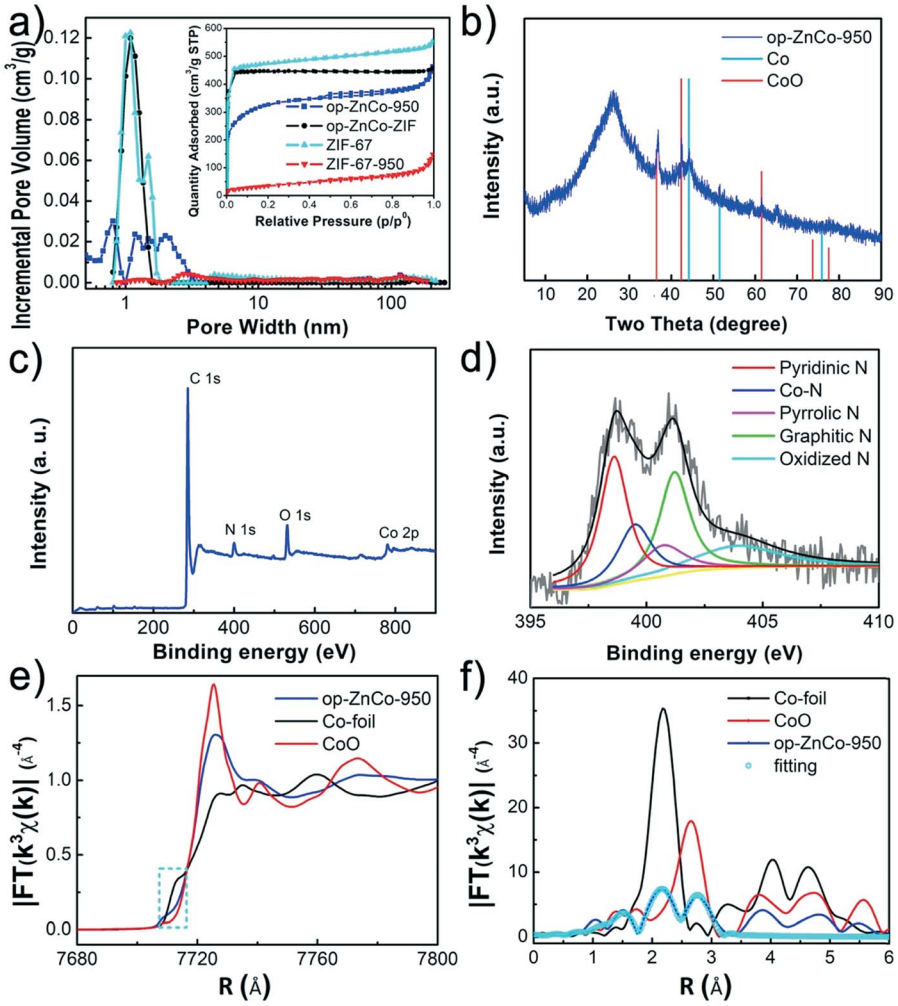

Fig. 3 (a) Pore size distribution and nitrogen adsorption-desorption isotherms (insert) of op-ZnCo-950, op-ZnCo-ZIF, ZIF-67 and ZIF-67-950. (b) PXRD graphs of op-ZnCo-950 and standard XRD peaks of Co (PDF#15-0806) and CoO (PDF#43-1004). (c) XPS spectra of op-ZnCo-950, and (d) corresponding deconvoluted N1s XPS spectrum. (e) XANES spectra and (f) k^3-weighted $\chi(k)$-function (Fourier-transformation) of Co K-edge spectra and the fitting curve of op-ZnCo-950 with standard Co-foil and CoO spectra.

content (4.23 at%) than ZIF-67-950 (1.15 at%), because the special core-shell structure is beneficial for preventing the loss of nitrogen. The high-resolution N1s spectrum of op-ZnCo-950 can be deconvoluted into five types of N (pyridinic N (398.6 eV), Co-N (399.5 eV), pyrrolic N (400.7 eV), graphitic N (401.2 eV), and oxidized N (403.9 eV)), as shown in Figure 3d. The contents are 30.5%, 16.3%, 11.0%, 26.0% and 16.2%, respectively.[65–67] We can find the pyridinic N and graphitic N occupy the predominant position. The contents of the five types of N are summarized in Table S3. On the contrary, it is hard to finely define the nitrogen types in ZIF-67-950 because of the low content, as shown in Figure S2.

Further metal coordination environment information about the Co/CoO NPs can be obtained by the X-ray absorption near-edge structure (XANES) and extended X-ray absorption fine structure (EXAFS), as shown in Figure 3e and 3f. The XANES spectrum of op-ZnCo-950 is located between those of Co foil and CoO because of the coexistence of Co NPs and CoO in op-ZnCo-950. There are three main peaks in the EXAFS spectrum of op-ZnCo-950. The first peak at about 1.5 Å is attributed to the isolated Co-N (O) bonds, while it is difficult to further distinguish the exact contribution from Co-N or Co-O. The second dominate peak of Co-Co bond appears at 2.16 Å, implying the presence of metallic Co. And the peak at 2.76 Å is in coincidence with Co-O-Co bond in CoO. The peak fitting and quantitative analysis of the EXAFS data was carried out by the IFEFFIT package with Co-foil and CoO as models. The fitting curve is shown in Figure S3, and the fitting results were summarized in Table S4. The coordination

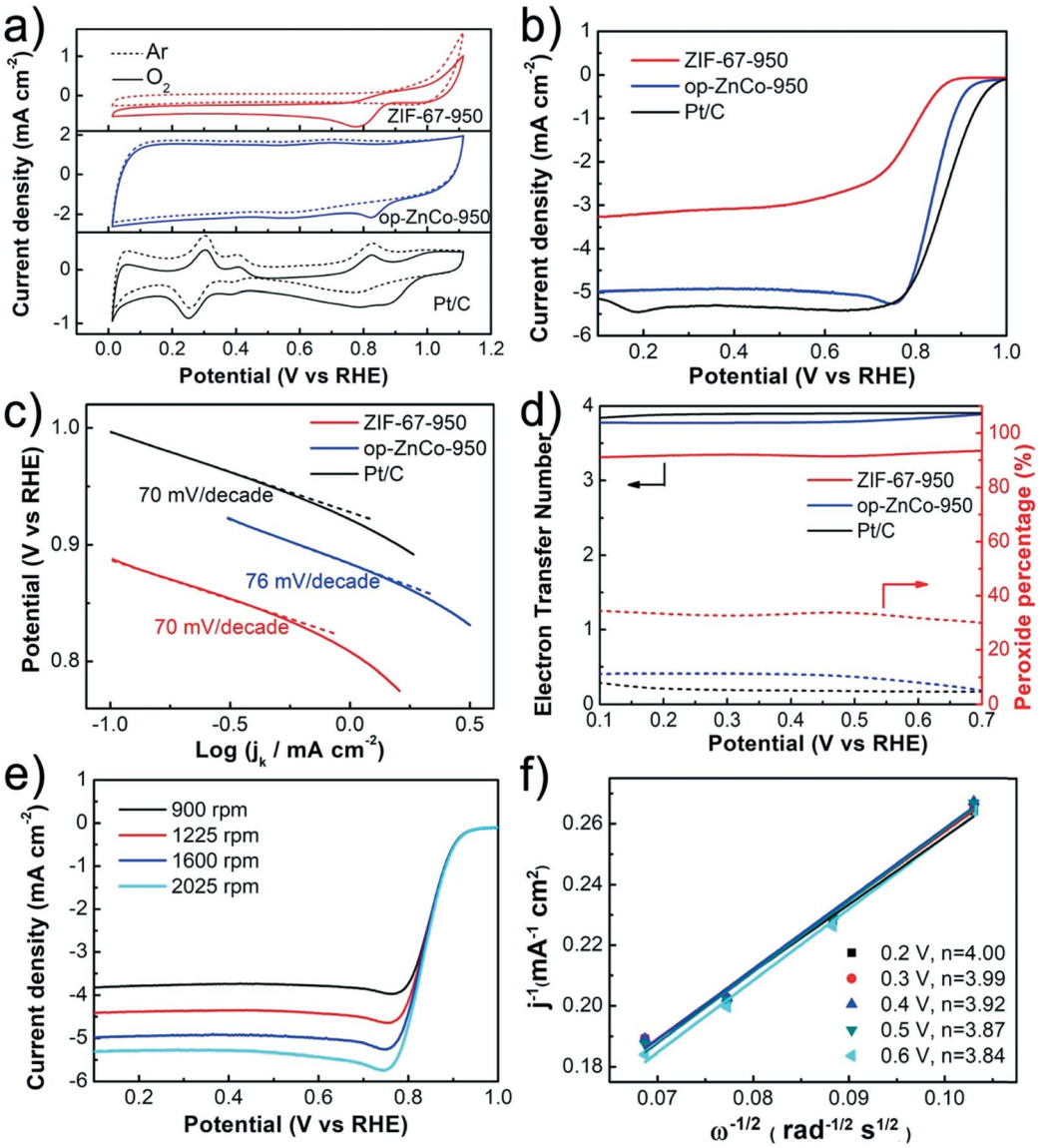

Fig. 4 (a) CV curves of op-ZnCo-950, ZIF-67-950 and commercial 20 wt% Pt/C in 0.1 M KOH solutions under Ar-saturated (dash line) and O_2-saturated (solid line) status at a sweep rate of 50 mV s^{-1}. (b) LSV curves of op-ZnCo-950, ZIF-67-950 and commercial 20 wt% Pt/C, in 0.1 M KOH, under oxygen bubbling at scan rate of 10 mV s^{-1} and electrode-rotating speed of 1600 rpm. (c) Corresponding Tafel plots obtained from the RDE polarozation curves. (d) The electron transfer numbers (*n*; black, leftside) and the peroxide yield (blue, rightside) of the three samples at potential range of 0.1 V to 0.7 V on the basis of RRDE voltammograms. (e) LSV curves of op-ZnCo-950 at different rotating speeds (900 rpm-2025 rpm) in O_2-saturated 0.1 M KOH. (f) Corresponding Koutecky-Levich plots of op-ZnCo-950 derived from LSV curves.

number of Co-N (O) in op-ZnCo-950 is 2.5 with the R factor of 0.014, revealing the existing possibility of Co-N_2, Co-N_3 and Co-O bond in the materials. Combining EXAFS results and HRTEM images, we believed that the Co/CoO NPs were coordinated with N-C or directly coordinated with C in graphitic carbon layers.

The above results indicate that the Co-based NPs consist Co and CoO simultaneously. Although the pyrolysis was carried out under inert gas atmosphere, slight oxidation may still occur in the materials after exposure to air. For example, low content of Co_3O_4 were detected after pyrolysis of CoZIF-VXC72.[43] And CoO/Co CNTs[68,69] were synthesized by one-step method from ZIF-12 under inert atmosphere. Here, we speculate that the O species come from the post surficial oxidation of Co NPs under the storage condition.

The ratio (I_D/I_G) of the peaks of D band (1353 cm^{-1}) and G band (1588 cm^{-1}) can be used to estimate the defected carbon structure or the graphitization degree of carbon materials. Raman spectra in Figure S4 shows that op-ZnCo-950 has a higher I_D/I_G (1.08) than ZIF-67-950 (1.01), indicating relative lower graphitization degree of op-ZnCo-950. The absence of 2D and D + G peaks in op-ZnCo-950 indicates more defects in carbon matrix of op-ZnCo-950, like Co-N-C and N-C.

The electrochemical measurements were carried out to reflect ORR activities of the samples in 0.1 M KOH aqueous solution at room temperature. In Figure 4a, the obvious cathodic peaks were detected for all the three samples in O_2-saturated solution, compared to the featureless curves of Ar-saturated solution, meaning their abilities for oxygen reduction. As displayed in Figure 4b, ZIF-67-950 shows the worst ORR activity among the three samples, while op-ZnCo-950 exhibits a comparable ORR activity with commercial 20 wt% Pt/C. Both its onset potential and half-wave potential (0.96 V, 0.846 V *vs* RHE) are close to those of 20 wt% Pt/C (0.99 V, 0.867 V *vs* RHE). In Figure 4c, op-ZnCo-950 shows a closer Tafel curve to 20 wt% Pt/C than ZIF-67-950. Both op-ZnCo-950 and ZIF-67-950 show similar Tafel slope with 20 wt% Pt/C, which means they have similar electrochemical kinetics, but op-ZnCo-950 shows a higher intercept which means a higher current density under the same potential than ZIF-67-950. Both the yield of H_2O_2 and electron transfer number (Figure 4d) derived from RRDE LSV curves (Figure S5) can reveal the inner electron transfer mechanism of the catalysts. H_2O_2, as the product of 2-electron reaction, is detrimental to catalysts. The low H_2O_2 yield (below 10%) of op-ZnCo-950 suggested that this catalyst possesses a high selectivity for 4-electron transfer pathway. Moreover, both RRDE LSV curves and K-L curves (derived from RDE LSV curves at different rotating speeds, Figure 4e) can be used to calculate the electron transfer number. The results by two methods are coincided with each other, in the range of 3.77~3.96 (Figure 4d, according to RRDE results) and 3.84~4.0 (Figure 4f, according to K-L plots). This also indicates that op-ZnCo-950 holds the preferred 4-electron transfer mechanism. For comparison, the LSV curves in different rotating speeds and the K-L plots of ZIF-67-950 and 20 wt% Pt/C were displayed in Figure S6. The electron transfer numbers calculated by K-L plots of op-ZnCo-950 are comparable with those of 20 wt% Pt/C and significant larger than ZIF-67-950, which well agrees with the results in Figure 4d.

In addition, the current-time chronoamperometric response (i-t curve) in Figure 5a shows the high stability of op-ZnCo-950 with nearly 95% retention, which is much higher than 85% retention of Pt/C after 20000 seconds. It may be attributed to the strong covalent bonds between C, N and Co, which can delay the degradation of op-ZnCo-950 catalysts. Moreover, the methanol tolerance and stability were also investigated using i-t curve. When methanol (3 mL) was injected into the electrolyte at 400 s, the i-t curve of Pt/C showed an obvious drop caused by the methanol oxidation reaction (Figure 5b), while there was almost no effect on the i-t curve of op-ZnCo-950. This suggests that op-ZnCo-950 has much higher methanol tolerance and stability than commercial 20 wt% Pt/C.

Considering the reasons of the high-performance ORR electrochemical activity of op-ZnCo-950, we believed that both active sites and mass transfer were pivotal. Op-ZnCo-950 possesses abundant and well-dispersed active sites, and hierarchical porous structure, which guarantees efficient mass transfer in the materials during the electrochemical reaction. Benefiting from the proper porous properties, the mass transport resistance decreased significantly, and the active sites therefore get exposed fully, which greatly enhances the ORR activity. On the contrary, the pores in ZIF-67-950 are blocked by the severe aggregation of Co NPs, which can be confirmed by the obviously smaller BET SSA (133.6 m^2 g^{-1}). The small BET SSA not only limits the mass transfer, but also blocks the exposure of the active sites.

The high activity of op-ZnCo-950 may be attributed to Co/CoO NPs, in which NPs connect with N-C bond or C adjacent to N. Previous investigations indicate that Co,[70] CoO[71] and Co-N[49] are positively beneficial for ORR. In fact, nitrogen content also plays an important role for ORR. As Nakamura *et al.*[72] claimed that those carbon atoms adjacent to pyridinic N were proved to be the active sites for ORR. And the graphitic N was also believed to promote the adsorption of oxygen atoms.[73] Importantly, the metal-N species provide most active sites for ORR.[37,49,74] So, the high content of pyridinic N, Co-N and graphitic N might be another important reason of the high activity of op-ZnCo-950 besides the good porous property.

4. Conclusions

In summary, a facile and effective one-pot approach has been proposed to synthesize a special precursor of core-shell ZIF-8@ZnCo-ZIF structure, by which we derived Co, N-doped porous carbon catalysts (op-ZnCo-950) by pyrolysis. The op-ZnCo-950 exhibits excellent electrocatalytic activity for ORR with a half-wave potential of 0.846 V (*vs* RHE). Moreover, op-ZnCo-950 catalyst also shows higher methanol resistance and better stability than commercial 20% Pt/C. The high electrocatalytic activity of op-ZnCo-950 could be attributed to the high content of nitrogen (mainly pyridinic N and graphitic N), uniformly distributed Co-based (including Co, Co-N and CoO) active sites and hierarchical pore structure and high BET surface area. These excellent properties of op-ZnCo-950 roots in the special core-shell precursor of op-ZnCo-ZIF, because the reduction and evaporation of Zn species in op-ZnCo-ZIF can produce the micropores and mesopores at high temperature, while the cobalt in the shell is therefore dispersed well into surface of samples, and maximal exposure of active sites can be achieved. It is expected the core-shell template strategy can provide an avenue to develop new catalysts for energy-related applications, including fuel cells, water splitting, supercapacitors or CO_2 electroreduction.

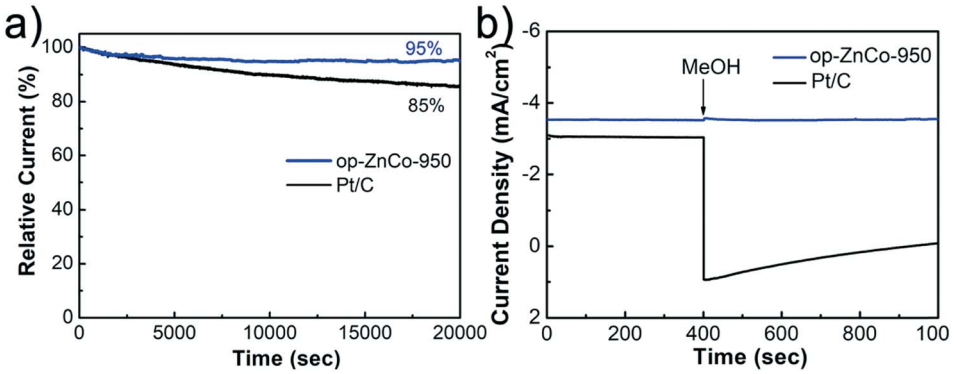

Fig. 5 (a) Current-time (i-t) chronoamperometric response of op-ZnCo-950 and 20 wt% Pt/C at -0.4 V (*vs* SCE) in O_2-saturated 0.1 M KOH at a rotating rate of 1000 rpm. (b) i-t chronoamperometric response of op-ZnCo-950 and 20 wt% Pt/C electrodes by adding 3 mL methanol after about 400 s.

Acknowledgements

This work is supported by National Science Fund for Distinguished Young Scholars (No. 21625601) and Outstanding Talent Fund from BUCT.

Conflicts of interest

There are no conflicts to declare.

Supporting information

Experimental details on synthesis and characterizations, including BET SSA, elemental contents of samples, the detailed EXAFS fitting curves, Raman spectra, RRDE polarization curves etc.

References

1 Y. Jiao, Y. Zheng, M. Jaroniec and S. Z. Qiao, *Chem. Soc. Rev.*, 2015, **44**, 2060–2086.
2 Y. Zhao, L. P. Wang, M. T. Sougrati, Z. X. Feng, Y. Leconte, A. Fisher, M. Srinivasan and Z. C. Xu, *Adv. Energy Mater.*, 2017, **7**, 1601424.
3 Z. L. Wang, D. Xu, H. X. Zhong, J. Wang, F. L. Meng and X. B. Zhang, *Sci. Adv.*, 2015, **1**, e1400035.
4 L. Yang, X. Zeng, D. Wang and D. Cao, *Energy Storage Mater.*, 2018, **12**, 277–283.
5 Y. Lv, L. Yang and D. Cao, *ACS Appl. Mater. Interfaces*, 2017, **9**, 32859–32867.
6 X. Xiang, F. Pan and Y. Li, *Adv. Compos. Hybrid Mater.*, 2017, **1**, 6–31.
7 L. Dai, Y. Xue, L. Qu, H. J. Choi and J. B. Baek, *Chem. Rev.*, 2015, **115**, 4823–4892.
8 C. Wei, L. Yu, C. Cui, J. Lin, C. Wei, N. Mathews, F. Huo, T. Sritharan and Z. Xu, *Chem. Comm.*, 2014, **50**, 7885–7888.
9 N. S. Porter, H. Wu, Z. Quan and J. Fang, *Acc. Chem. Res.*, 2013, **46**, 1867–1877.
10 Y. Nie, L. Li and Z. Wei, *Chem. Soc. Rev.*, 2015, **44**, 2168–2201.
11 Y. Hu, J. O. Jensen, W. Zhang, L. N. Cleemann, W. Xing, N. J. Bjerrum and Q. Li, *Angew. Chem. Int. Ed.*, 2014, **53**, 3675–3679.
12 Y. Deng, Y. Dong, G. Wang, K. Sun, X. Shi, L. Zheng, X. Li and S. Liao, *ACS Appl. Mater. Interfaces*, 2017, **9**, 9699–9709.
13 B. You, N. Jiang, M. L. Sheng, W. S. Drisdell, J. Yano and Y. J. Sun, *ACS Catal.*, 2015, **5**, 7068–7076.
14 Z. J. Wang, Y. Z. Lu, Y. Yan, T. Y. P. Larissa, X. Zhang, D. Wuu, H. Zhang, Y. H. Yang and X. Wang, *Nano Energy*, 2016, **30**, 368–378.
15 M. Dou, D. He, W. Shao, H. Liu, F. Wang and L. Dai, *Chem. Eur. J.*, 2016, **22**, 2896–2901.
16 K. Ai, Z. Li and X. Cui, *J. Power Sources*, 2017, **368**, 46–56.
17 Y. Han, Y. G. Wang, W. Chen, R. Xu, L. Zheng, J. Zhang, J. Luo, R. A. Shen, Y. Zhu, W. C. Cheong, C. Chen, Q. Peng, D. Wang and Y. Li, *J. Am. Chem. Soc.*, 2017, **139**, 17269–17272.
18 L. Huang, X. Zhang, Y. Han, Q. Wang, Y. Fang and S. Dong, *J. Mater. Chem. A*, 2017, **5**, 18610–18617.
19 J. Xiao, C. Zhao, C. Hu, J. Xi and S. Wang, *J. Power Sources*, 2017, **348**, 183–192.
20 Y. Ye, H. Li, F. Cai, C. Yan, R. Si, S. Miao, Y. Li, G. Wang and X. Bao, *ACS Catal.*, 2017, **7**, 7638–7646.
21 Y. Zheng, Y. Jiao, Y. Zhu, Q. Cai, A. Vasileff, L. H. Li, Y. Han, Y. Chen and S. Z. Qiao, *J. Am. Chem. Soc.*, 2017, **139**, 3336–3339.
22 Y. Guo, P. Yuan, J. Zhang, Y. Hu, I. S. Amiinu, X. Wang, J. Zhou, H. Xia, Z. Song, Q. Xu and S. Mu, *ACS Nano*, 2018, **12**, 1894–1901.
23 M. Kuang, Q. Wang, P. Han and G. Zheng, *Adv. Energy Mater.*, 2017, **7**, 1700193.
24 X. Ma, X. Zhao, J. Huang, L. Sun, Q. Li and X. Yang, *ACS Appl. Mater. Interfaces*, 2017, **9**, 21747–21755.
25 L. Yang, Y. Lv and D. Cao, *J. Mater. Chem. A*, 2018, **6**, 3926–3932.
26 M. Wang, L. Guo and D. Cao, *Sens. Actuators B Chem.*, 2018, **256**, 839–845.
27 M. Wang, L. Guo and D. Cao, *Anal. Chem.*, 2018, **90**, 3608–3614.
28 L. Yang, X. Zeng, W. Wang and D. Cao, *Adv. Funct. Mater.*, 2018, **28**, 1704537.
29 P. Zhang, F. Sun, Z. H. Xiang, Z. G. Shen, J. Yun and D. Cao, *Energy Environ. Sci.*, 2014, **7**, 442–450.
30 M. Jahan, Z. L. Liu and K. P. Loh, *Adv. Funct. Mater.*, 2013, **23**, 5363–5372.
31 H. Wang, F. X. Yin, G. R. Li, B. H. Chen and Z. Q. Wang, *Int. J. Hydrogen Energy*, 2014, **39**, 16179–16186.
32 H. Wang, F. X. Yin, B. H. Chen, X. B. He, P. L. Lv, C. Y. Ye and D. J. Liu, *Appl. Catal. B-Environ.*, 2017, **205**, 55–67.
33 S. Xu, Y. Lv, X. Zeng and D. Cao, *Chem. Eng. J.*, 2017, **323**, 502–511.
34 L. N. Chong, G. A. Goenaga, K. Williams, H. M. Barkholtz, L. R. Grabstanowicz, J. A. Brooksbank, A. B. Papandrew, R. Elzein, R. Schlaf, T. A. Zawodzinski, J. X. Zou, S. Q. Ma and D. J. Liu, *ChemElectroChem*, 2016, **3**, 1541–1545.
35 H. X. Zhong, J. Wang, Y. W. Zhang, W. L. Xu, W. Xing, D. Xu, Y. F. Zhang and X. B. Zhang, *Angew. Chem. Int. Ed.*, 2014, **53**, 14235–14239.
36 W. Zhang, Z. Y. Wu, H. L. Jiang and S. H. Yu, *J. Am. Chem. Soc.*, 2014, **136**, 14385–14388.
37 W. Xia, J. H. Zhu, W. H. Guo, L. An, D. G. Xia and R. Q. Zou, *J. Mater. Chem. A*, 2014, **2**, 11606–11613.
38 S. Wang, Z. Cui and M. Cao, *Chem. Eur. J.*, 2015, **21**, 2165–2172.
39 D. Zhao, J. L. Shui, C. Chen, X. Q. Chen, B. M. Reprogle, D. P. Wang and D. J. Liu, *Chem. Sci.*, 2012, **3**, 3200–3205.
40 P. Yin, T. Yao, Y. Wu, L. Zheng, Y. Lin, W. Liu, H. Ju, J. Zhu, X. Hong, Z. Deng, G. Zhou, S. Wei and Y. Li, *Angew. Chem. Int. Ed.*, 2016, **55**, 10800–10805.
41 D. Zhao, J. L. Shui, L. R. Grabstanowicz, C. Chen, S. M. Commet, T. Xu, J. Lu and D. J. Liu, *Adv. Mater.*, 2014, **26**, 1093–1097.
42 B. Y. Guan, X. Y. Yu, H. B. Wu and X. W. D. Lou, *Adv. Mater.*, 2017, 1703614.
43 B. Ni, C. Ouyang, X. Xu, J. Zhuang and X. Wang, *Adv. Mater.*, 2017, **29**, 1701354.

44 H. Wang, Q.-L. Zhu, R. Zou and Q. Xu, *Chem*, 2017, **2**, 52–80.

45 H. Yu, A. Fisher, D. Cheng and D. Cao, *ACS Appl. Mater. Interfaces*, 2016, **8**, 21431–21439.

46 S. Gadipelli and Z. X. Guo, *ChemSusChem*, 2015, **8**, 2123–2132.

47 X. Chen, K. Shen, J. Chen, B. Huang, D. Ding, L. Zhang and Y. Li, *Chem. Eng. J.*, 2017, **330**, 736–745.

48 L. Ge, Y. Yang, L. Wang, W. Zhou, R. De Marco, Z. Chen, J. Zou and Z. Zhu, *Carbon*, 2015, **82**, 417–424.

49 S. Ma, G. A. Goenaga, A. V. Call and D. J. Liu, *Chem. Eur. J.*, 2011, **17**, 2063–2067.

50 H. Wang, F. Yin, P. Lv, T. Fan, X. He and B. Chen, *Int. J. Hydrogen Energy*, 2017, **42**, 2127–2133.

51 H. Hu, L. Han, M. Yu, Z. Wang and X. W. Lou, *Energy Environ. Sci.*, 2016, **9**, 107–111.

52 X. J. Wang, J. W. Zhou, H. Fu, W. Li, X. X. Fan, G. B. Xin, J. Zheng and X. G. Li, *J. Mater. Chem. A*, 2014, **2**, 14064–14070.

53 X. J. Wang, X. X. Fan, H. H. Lin, H. Fu, T. Wang, J. Zheng and X. G. Li, *RSC Adv.*, 2016, **6**, 37965–37973.

54 X. Song, L. Guo, X. Liao, J. Liu, J. Sun and X. Li, *Small*, 2017, **13**, 1700238.

55 Y. Z. Chen, C. Wang, Z. Y. Wu, Y. Xiong, Q. Xu, S. H. Yu and H. L. Jiang, *Adv. Mater.*, 2015, **27**, 5010–5016.

56 S. S. A. Shah, L. Peng, T. Najam, C. Cheng, G. Wu, Y. Nie, W. Ding, X. Qi, S. Chen and Z. Wei, *Electrochim. Acta*, 2017, **251**, 498–504.

57 M. Xiao, J. Zhu, L. Ma, Z. Jin, J. Ge, X. Deng, Y. Hou, Q. He, J. Li, Q. Jia, S. Mukerjee, R. Yang, Z. Jiang, D. Su, C. Liu and W. Xing, *ACS Catal.*, 2018, **8**, 2824–2832.

58 H. Zhang, S. Hwang, M. Wang, Z. Feng, S. Karakalos, L. Luo, Z. Qiao, X. Xie, C. Wang, D. Su, Y. Shao and G. Wu, *J. Am. Chem. Soc.*, 2017, **139**, 14143–14149.

59 Y. Pan, K. Sun, S. Liu, X. Cao, K. Wu, W. C. Cheong, Z. Chen, Y. Wang, Y. Li, Y. Liu, D. Wang, Q. Peng, C. Chen and Y. Li, *J. Am. Chem. Soc.*, 2018, **140**, 2610–2618.

60 J. Meng, C. Niu, L. Xu, J. Li, X. Liu, X. Wang, Y. Wu, X. Xu, W. Chen, Q. Li, Z. Zhu, D. Zhao and L. Mai, *J. Am. Chem. Soc.*, 2017, **139**, 8212–8221.

61 J. Tang, R. R. Salunkhe, J. Liu, N. L. Torad, M. Imura, S. Furukawa and Y. Yamauchi, *J. Am. Chem. Soc.*, 2015, **137**, 1572–1580.

62 J. Zhang, T. Zhang, K. Xiao, S. Cheng, G. Qian, Y. Wang and Y. Feng, *Cryst. Growth Des.*, 2016, **16**, 6494–6498.

63 R. Banerjee, A. Phan, B. Wang, C. Knobler, H. Furukawa, M. O'Keeffe and O. M. Yaghi, *Science*, 2008, **319**, 939–943.

64 T. Chen, B. Cheng, G. Zhu, R. Chen, Y. Hu, L. Ma, H. Lv, Y. Wang, J. Liang, Z. Tie, Z. Jin and J. Liu, *Nano Lett.*, 2017, **17**, 437–444.

65 S. Kabir, K. Artyushkova, B. Kiefer and P. Atanassov, *Phys. Chem. Chem. Phys.*, 2015, **17**, 17785–17789.

66 K. Artyushkova, B. Kiefer, B. Halevi, A. Knop-Gericke, R. Schlogl and P. Atanassov, *Chem. Commun.*, 2013, **49**, 2539–2541.

67 A. Serov, K. Artyushkova and P. Atanassov, *Adv. Energy Mater.*, 2014, **4**, 1301735.

68 I. A. Khan, F. Nasim, M. Choucair, S. Ullah, A. Badshah and M. A. Nadeem, *RSC Adv.*, 2016, **6**, 1129–1135.

69 I. A. Khan, A. Badshah and M. A. Nadeem, *Catal. Commun.*, 2017, **99**, 10–14.

70 B. Y. Xia, Y. Yan, N. Li, H. B. Wu, X. W. Lou and X. Wang, *Nat. Energy*, 2016, **1**, 15006.

71 S. Guo, S. Zhang, L. Wu and S. Sun, *Angew. Chem. Int. Ed.*, 2012, **51**, 11770–11773.

72 D. H. Guo, R. Shibuya, C. Akiba, S. Saji, T. Kondo and J. Nakamura, *Science*, 2016, **351**, 361–365.

73 S. Wang, Z. Cui and M. Cao, *Electrochim. Acta*, 2016, **210**, 328–336.

74 Y. Zhou and J. Wang, *Nano Adv.*, 2017, **2**, 45–46.